

Author Query Form

Book title: (M39) The Eruption of Soufrière Hills Volcano, Montserrat from 2000 – 2010

Author: D. Delle Donne et al.

Chapter: 09

The following queries have arisen during copy-editing your manuscript. Please provide an answer in the right-hand column below and on your proofs. Many thanks for your help.

Query No.	Query	Response
Q1	Please check this proof carefully for other errors because once it is published online the only further change will be the addition of page numbers. In particular, check that figures, tables and equations are correct. Also, please check your proof to ensure you have acknowledged your funding source (if applicable).	
Q2	Please check that the meaning of this sentence has not been changed.	
Q3	We have changed Druitt et al. 2003 to Druitt et al. 2002 as per the References, is this correct? If not, please insert full publication details of Druitt et al. 2003 into the References and delete here.	
Q4	Are these velocities a range (i.e. 20 to 55–75 m s ⁻¹)? Please clarify the meaning here.	
Q5	Please cite Garces et al. 1999 in the text or delete here.	

Chapter 9

Thermal, acoustic and seismic signals from pyroclastic density currents and Vulcanian explosions at Soufrière Hills Volcano, Montserrat

D. DELLE DONNE¹, M. RIPEPE^{1*}, S. DE ANGELIS², P. D. COLE^{3,4},
G. LACANNA¹, P. POGGI⁵ & R. STEWART⁴

¹*Dipartimento Scienze della Terra, Università di Firenze, via G. La Pira, 4, 50121 Firenze, Italy*

²*Geophysical Institute University of Alaska Fairbanks 903 Koyukuk Drive, Fairbanks, AK 99775-7320, USA*

³*Montserrat Volcano Observatory, Flemmings, Montserrat, West Indies*

⁴*Seismic Research Centre, The University of the West Indies, St Augustine, Trinidad & Tobago, West Indies*

⁵*INO (Istituto Nazionale di Ottica), Largo E. Fermi, 6, 50125 Firenze, Italy*

*Corresponding author (e-mail: maurizio.ripepe@unifi.it)

Abstract: We show two examples of how integrated analysis of thermal and infrasound signal can be used to obtain, in real time, information on volcanic activity. Soufrière Hills Volcano (SHV) on Montserrat offers the opportunity to study a large variety of processes related to lava-dome activity, such as pyroclastic density currents (PDCs) and large Vulcanian eruptions. Infrasound and thermal analysis are used to constrain the propagation of PDCs and their velocities, which are calculated here to range between 15 and 75 m s⁻¹. During the Vulcanian eruption of 5 February 2010, infrasound and thermal records allow us to identify an approximately 13 s seismic precursor possibly related to the pressurization of the conduit before the explosion onset. The associated very long period (VLP) seismic signal is correlated with the gas-thrust phase detected by thermal imagery, and may reflect change in the upwards momentum induced by the mass discharge. Moreover, from infrasound and thermal analysis, we estimate a gas-thrust phase lasting 22 s, with an initial plume velocity of approximately 170 m s⁻¹ and a mean volumetric discharge rate of 0.3×10^5 – 9.2×10^5 m³ s⁻¹. This information provided in real time gives important input parameters for modelling the tephra dispersal into the atmosphere.

Lava-dome eruptions represent a style of volcanism of distinctive interest because of their potential consequences, such as the generation of pyroclastic density currents (PDCs) down the volcano's flanks and large explosive eruptions following partial-dome collapse. Lava domes are formed by silica-rich lava that is too viscous to flow and, instead, builds-up over the point of extrusion. The hazards from lava-dome eruptions are well known owing to unpredictable transitions from the slow extrusion of viscous lava to vigorous explosions, and to the propensity of lava domes to suddenly collapse, spawning devastating PDCs down the flanks of volcanic edifices (Young *et al.* 1998; Sparks & Young 2002). As a lava dome grows, parts of it may collapse because of gravitational instability or as the result of gas explosions within the dome itself, thus forming PDCs. The ability to detect and track the propagation of these fast-moving density currents is of utmost importance in understanding the evolution of lava-dome eruptions and mitigating related hazards.

Methods for the location of PDCs, based on seismic amplitudes, have been proposed in the past (e.g. Jolly *et al.* 2002) and have proved quite effective for the characterization of large collapse events. These techniques require dense seismic networks and optimal azimuthal coverage; both conditions are rarely met on lava dome volcanoes where seismic networks are sparse because of the restrictions imposed by rough terrain and eruption hazards. The use of seismic amplitudes requires understanding of local site effects and frequency-dependent attenuation, thus introducing another layer of complexity. Finally, these methods are not designed for unsupervised application in real-time; events classification and location require visual inspection of the seismograms, and manual intervention of a seismic analyst.

Ripepe *et al.* (2009) recently demonstrated the use of infrasound array technology to detect and track the evolution of PDC activity in real time. In this chapter we extend their work by introducing methods based on the integrated analyses of thermal imagery and an infrasound array data to evaluate, with unprecedented

resolution, the propagation velocity of PDCs. We show our results are in good agreement with predictions from theoretical models.

We use a thermo-acoustic method to constrain the duration of the gas-thrust phase, and the plume exit velocities at the vent during a Vulcanian eruption. Here we show how the integrated infrasound and thermal analysis for a large Vulcanian eruption that occurred at Soufrière Hills Volcano (SHV) on 5 February 2010 helps to better understand the associated seismic signal. Our aim is also to give an estimate of the plume exit velocity and volume flux that are important input parameters for the tephra dispersal predictive models evaluating the amount of volcanic ash emitted into the atmosphere.

Thermal camera and infrasonic array at MVO

A thermal camera and an infrasound array (Fig. 9.1) were co-located at Montserrat Volcano Observatory (MVO) at a distance of approximately 5.6 km from SHV. The camera is a FLIR A20 model, and is equipped with 34° × 25° optical lens of 9.2 mm and a maximum thermal resolution of 0.1 °C in the 7.5–13 μm wavelength interval. The camera field of view (FOV) above SHV is approximately 3.5 × 2.5 km, and it allows monitoring of both PDC activity towards the west (Plymouth), the NE (Old Airport) and to the north (Tyre's Ghaut and Belham Valley) as well as the explosive activity (Fig. 9.1). The thermal image acquisition and processing system has been designed to fulfil the specific needs of the MVO personnel, and is able to process, in real time, the large 352 × 244 pixel thermal images at two frames s⁻¹. A global positioning system (GPS) time-stamp on each frame allows synchronization with all other sensors recorded by the MVO seismic network (Luckett *et al.* 2007). This allows successful integration of thermal camera information within the MVO monitoring network, thus assisting observatory

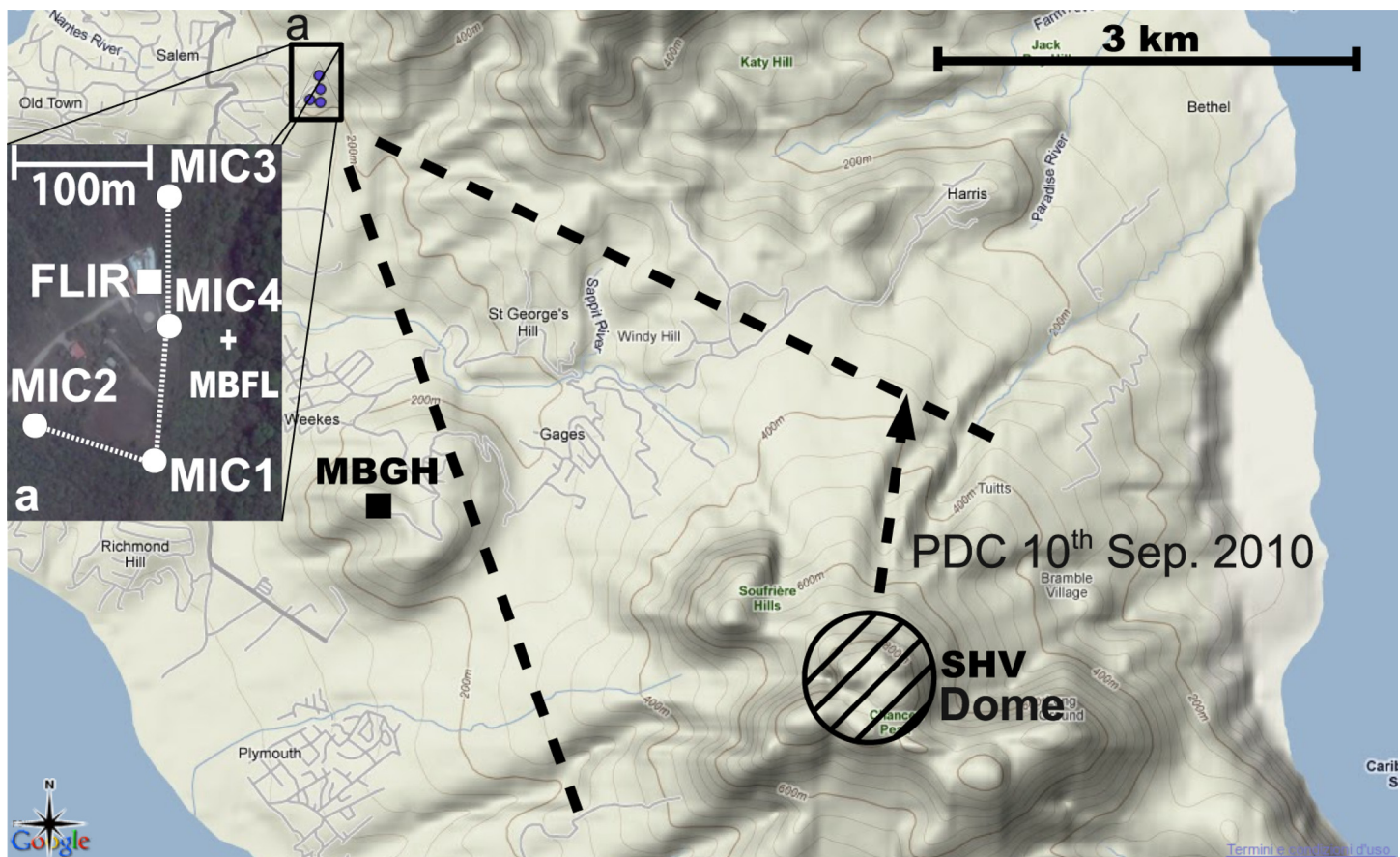


Fig. 9.1. Map with the position of the infrasonic array (MIC1, MIC2, MIC3 and MIC4), thermal camera (FLIR) and seismic-acoustic stations (MBFL and MBGH). The FOV of the thermal camera and the trajectory of the 10 September 2010 PDC are also shown with dashed lines.

staff with decision making during volcanic crises. This could include providing advice to local authorities about the ongoing eruptive activity, and prompting the evacuation of local population from areas potentially at risk from PDCs.

Volcanic activity is also monitored by an infrasonic array installed close to the MVO (Fig. 9.1) and at the same distance, approximately 5600 m, from the SHV lava dome. The array has a four-element 'L' geometry, with a total aperture of 220 m. Each element of the array is equipped with 'Item-prs' differential pressure transducers, with a sensitivity of 25 mV Pa^{-1} at 1 Hz, 250 Pa of full-scale range, a flat instrument response in the frequency band of 0.01–100 Hz, and a noise level of 10^{-2} Pa. The infrasonic signals are digitized with a resolution of 16 bits at 50 Hz sampling rate. The satellite sensors are connected to the receiver unit by fibre-optic cables. The use of fibre-optic technology provides an optimal signal-to-noise ratio (SNR), and protects the network from lightning hazards. Data are sent via RS-232 to the MVO where they are also processed in real time, archived and broadcast via the Internet (Ripepe *et al.* 2010).

Thermal image processing

Thermal imagery is processed measuring both the propagation vector field of PDCs and the upwards velocities of the tephra-plume. This is accomplished by: (1) converting thermal pixels to metres; (2) back-projecting pixels to the topography using a digital elevation model (DEM); and (3) tracking the vertical and horizontal propagation of the thermal anomalies associated with PDCs and volcanic plumes in successive frames.

The processing used is based on the thermal analysis method of single images. This method analyses the propagation front at

different temperature levels (Marchetti *et al.* 2009; Pistolesi *et al.* 2011; Delle Donne & Ripepe 2012). In summary, thermal images, $I_t(t, x, y)$ are converted into binary images, $I_b(t, x, y)$ (Fig. 9.2) according to the following formulae:

$$I_b(t, x, y) \begin{cases} 1, I_t(t, x, y) > T_{\text{bkg}} \\ 0, I_t(t, x, y) \leq T_{\text{bkg}} \end{cases} \quad (1)$$

where T_{bkg} is the ambient background temperature. Thus, for each frame $I_t(t)$ we obtain the distribution (x, y) of pixels characterized by temperatures higher than the background T_{bkg} and consider that they are related to volcanic material (e.g. pyroclasts, juvenile ash). It is worth noting that the temperatures given by thermal images are apparent because the cores of PDCs or volcanic plumes can be masked by the cloud exterior. We then estimate the high-temperature pixel distribution in the vertical, V_d , and horizontal, H_d , axis by adding up all the pixels, I_b , along the same row and for each column of the image (Fig. 9.2):

$$\begin{aligned} V_d(t, x) &= \sum_{y=1}^{y=Y} I_b(t, x, y) \\ H_d(t, y) &= \sum_{x=1}^{x=X} I_b(t, x, y) \end{aligned} \quad (2)$$

where X and Y are the horizontal (352 pixels) and the vertical (244 pixels) size of the image, respectively. $V_d(t, x)$ and $H_d(t, y)$ are the distribution functions representing the number of pixels with temperature above T_{bkg} along every horizontal and vertical line in the FOV, and thus represent the extension of the

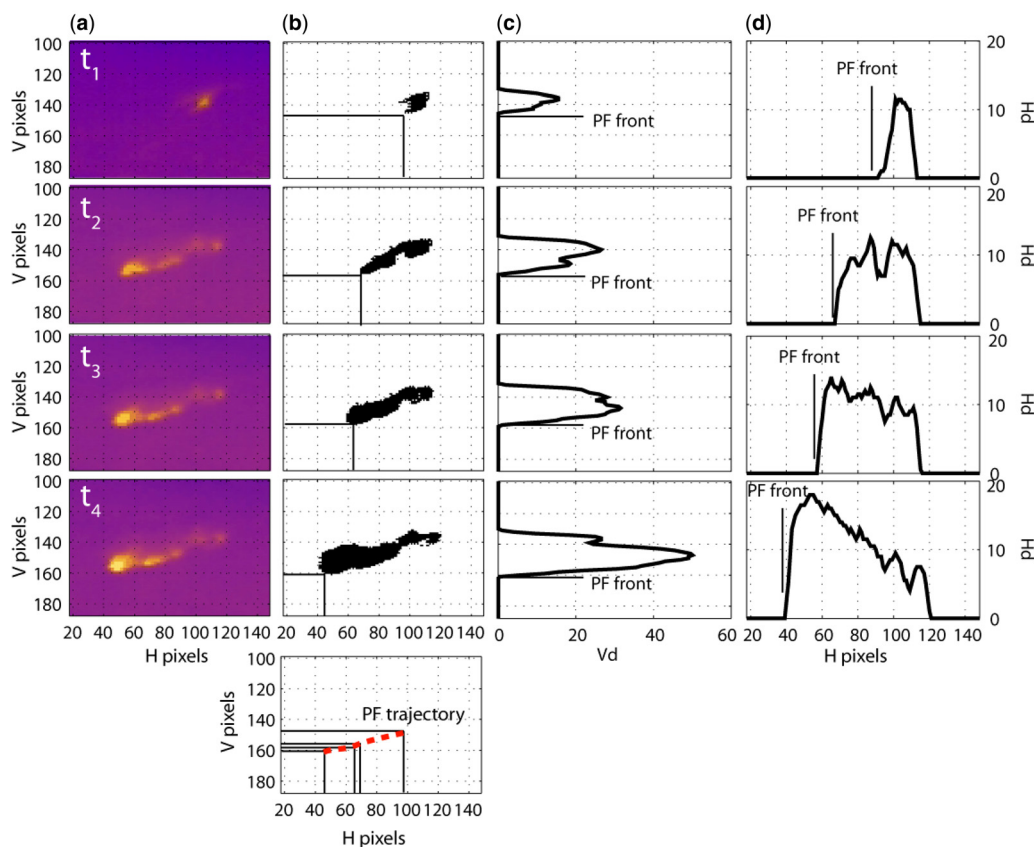


Fig. 9.2. PDC tracking methodology. (a) Original thermal images captured at the t_1-t_4 time interval are converted into (b) binary images using a background temperature threshold and allowing us to detect high-temperature areas in the FOV. Image decomposition method along (c) vertical and (d) horizontal axes allows tracking of the front of the high-temperature anomaly. (e) The trajectory is computed using information along both the horizontal and vertical directions.

Colour
online/
colour
hardcopy

high-temperature areas in the two directions. This analysis enables tracking the front of the thermal anomaly in the vertical and horizontal directions by picking the pixel coordinates where the distribution functions $V_d(t, x)$ and $H_d(t, y)$ increase (Fig. 9.2). Combining the information from the vertical and horizontal components, it is possible to calculate the apparent trajectory of the thermal anomaly (Fig. 9.2).

In order to calculate the propagation velocity of the thermal front, we convert pixel coordinates into metres by georeferencing the thermal images using five reference points with known geographical coordinates that are present and easily recognizable in the thermal image. We use the ‘Thin plate smoothing spline’ interpolation algorithm (Bookstein 1989) in order to produce a new ‘warped’ georeferenced image linked to the five reference points (Fig. 9.3). This georeferencing procedure is known as the non-rigid transformation model. Error in the warping method is not constant over the entire image, but depends on the distance from the reference points. Assuming that close to the reference points the error is small, to minimize the warping error, reference points have been selected over most of the image and as close as possible to the PDCs area. However, the topography around the dome changes rapidly with time and a reliable DEM is not always available. For this reason the velocities derived by our thermal imagery should not be considered as absolute velocities but rather as indicative of the mean velocity of the PDC front. The error in the velocity estimates depends on the pixel size of the thermal images ($c. 10$ m at a distance of 5600 m from the vent) and frame rate (2 Hz = 0.5 s). As a result, the instantaneous velocity has a maximum error of ± 10 m s $^{-1}$. Figure 9.3 shows how the georeferenced thermal images appear once they have been projected onto Google Earth by using the default 3 arcsecond ($3'$) ($c. 100$ m) DEM available on Google Earth software. This procedure permits projection of two-dimensional (2D) thermal images onto 3D topography to precisely locate the position of the thermal front draped on topography. This is an extremely useful tool if integrated into the monitoring and alert system

because it permits real-time location of the extension and propagation of the PDCs.

Infrasound array processing

During explosions, such as those that have occurred at SHV, infrasound is produced by volumetric sources rapidly expanding into the atmosphere, but it is also formed by non-explosive sources related to dome collapses, such as PDCs, rockfalls and lahars.

The permanent small-aperture (220 m) four-element infrasonic array, such as that deployed at the MVO, has proved its ability to detect both point sources, such as explosive events, and non-point moving sources, such as PDCs and debris flows, in real-time (Ripepe *et al.* 2010). Source location is based on the assumption that a signal is coherent at the different sensors, whereas noise is not correlated. The array processing applies multichannel correlation using a grid-searching method to identify signals from noise in terms of wave propagation back-azimuth and apparent velocity. The propagation back-azimuth indicates the direction of the signal source. Assuming that infrasound reaches the array as a planar wave front, with 90° incident angle (from the vertical) at constant velocity, infrasonic waves should propagate across the array at the same speed of sound ($c. 340$ m s $^{-1}$), which depends primarily on air temperature and, to a small extent, on humidity. This assumption of plane-wave propagation is justified as the source–receiver distance of approximately 5600 m is considerably larger than the 220 m aperture of the array.

The apparent velocity is the velocity that the wave will have when it is not travelling in the same plane, as defined by the array; that is, with an incident angle $< 90^\circ$. High apparent velocities (> 340 m s $^{-1}$) will thus be related to lower incident angles ($< 90^\circ$) and, therefore, to a source located above the array plane. It is worth noting that the maximum difference in elevation between sensors is 30 m over 220 m of aperture, so that the ideal

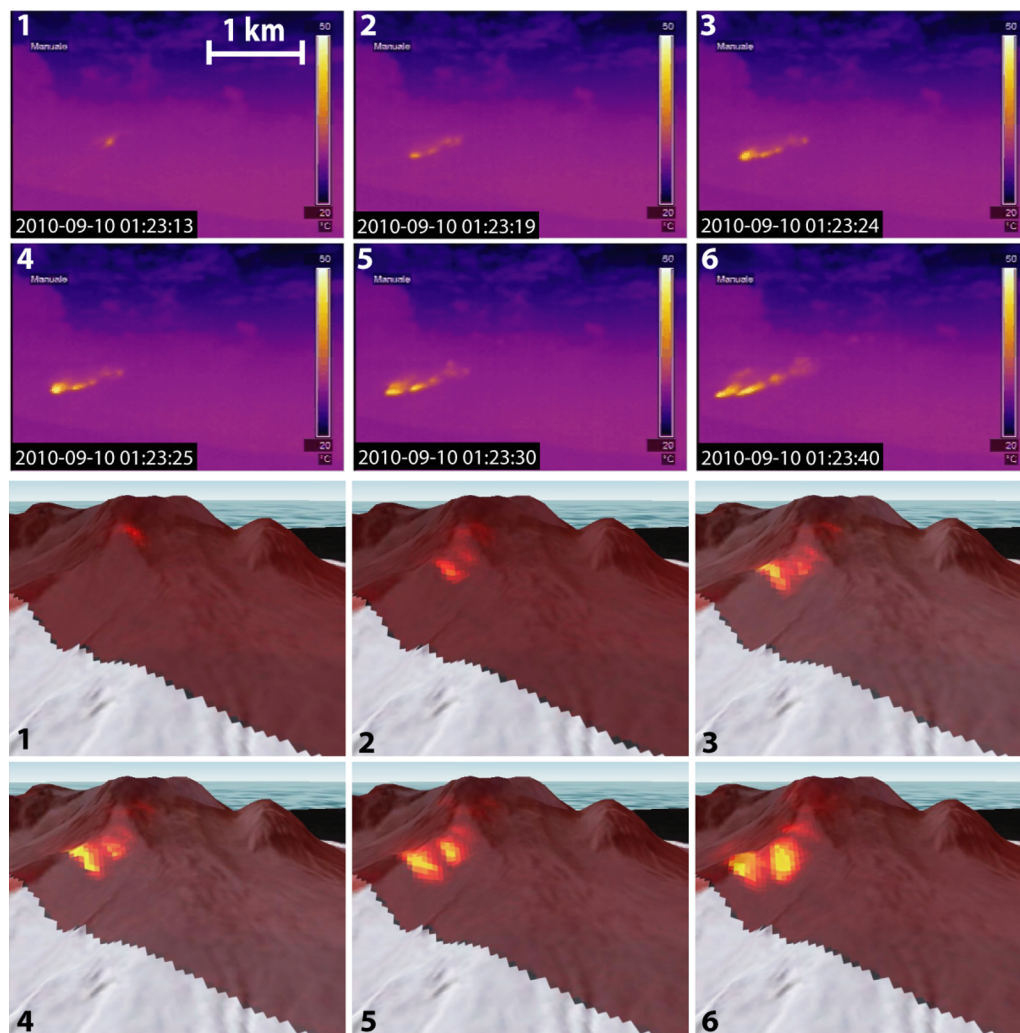


Fig. 9.3. Six snapshots associated with the PDC that occurred on 10 September 2010 and running towards the NE along the collapse scar produced by the 11 February 2010 partial dome collapse, as detected by the FLIR thermal camera and associated 3D Google Earth view after thin smoothing spline georeferentiation.

Colour
online/
colour
hardcopy

plane defined by the array is very close to the horizontal. Variation in apparent velocity will indicate a change in the altitude and, hence, a moving source. Furthermore, high apparent velocities ($>400 \text{ m s}^{-1}$) correspond to steep incident angles that represent unrealistic sources originating from the volcano.

The degree of signal correlation across the array is controlled by the time residual. The time residual is the sum of the delays between three array sensor pairs calculated in real time by multiple cross-correlation. Highly correlated signals (>0.8) have a time residual approaching 0. This procedure (see Ulivieri *et al.* 2011 among others) is performed for all the possible triplets of sensors of the array, and we consider a detection to be valid if the mean of time residuals is below the consistency threshold of 0.015 s, which corresponds to a 70% correlation for a signal with a peak frequency of 1 Hz. The propagation back-azimuth and apparent velocity is calculated as the mean value between all the possible combination of sensors within the different triplets using the distances and the time delays, and assuming a constant propagation velocity (see Cansi 1995; Ulivieri *et al.* 2011 for details). The accuracy of the array back-azimuth depends on the array aperture, sampling rate, frequency content of the infrasonic signal and the signal-to-noise ratio. For a 220 m aperture array and considering a frequency content of 1 Hz, typical of infrasound generated by volcanic activity, the expected azimuth resolution is of approximately 0.9° , which corresponds to 88 m at 5600 m of slant distance.

The use of a small-aperture infrasonic array improves the capabilities of volcano observatories for monitoring activities during eruption crises (e.g. Ripepe *et al.* 2007; Johnson & Ripepe 2011), and also provides useful corroboration for other

geophysical parameters (mainly seismic signals, ground visible and thermal cameras, and gas monitoring) (Garces *et al.* 2000; Vergnolle & Caplan-Auerbach 2006; Johnson 2007).

This location procedure is performed in real time using 5 s moving windows with 90% overlap on all possible triplets of sensors in the array, and allows detection and tracking of infrasound generated by PDCs. Once a coherent arrival across the array is detected, we use back-azimuth and incident angle information to map the source onto the DEM.

Thermo-acoustic tracking of the propagation of PDCs

The propagation of the PDCs is mainly controlled by three parameters: topography, basal friction angle (an empirical property of two contacting materials) and initial velocity. While the topography is well known, and the basal friction angle can be estimated to be of the order of 12° – 16.5° (Nikolkina *et al.* 2011), data of initial velocities of the PDCs from the SHV are poorly documented. Average velocities of propagation have been measured in the range of 5 – 35 m s^{-1} (Calder *et al.* 2002; Cole *et al.* 2002; Carn *et al.* 2004), but modelling suggests that initial velocities of dome-collapse-induced PDCs can be much higher, reaching approximately 50 – 70 m s^{-1} (Wadge *et al.* 1998; Calder *et al.* 1999; Hooper & Mattioli 2001). The estimation of propagation velocity of PDCs is crucial to estimating hazards as velocity controls the run-out and the extents of the affected area of the PDC.

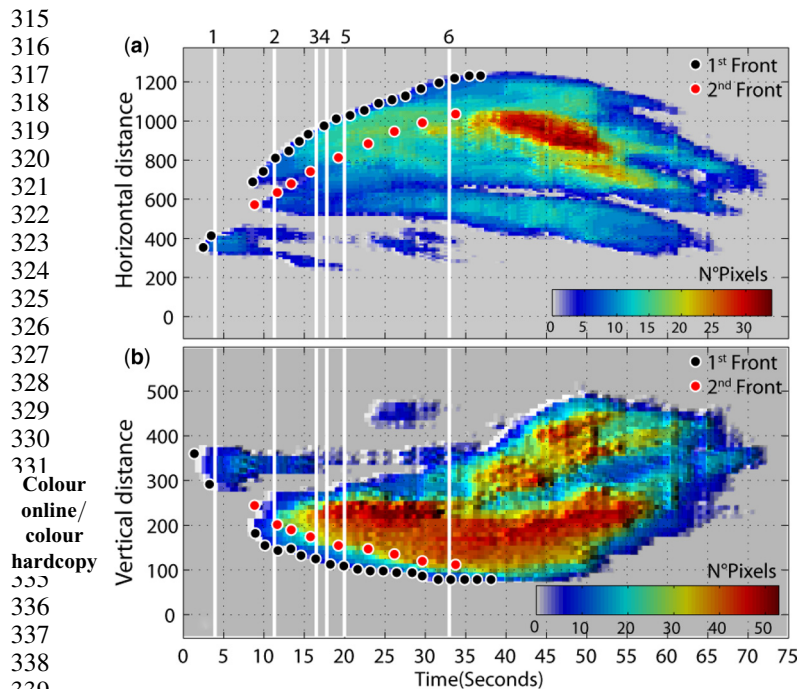
The combined thermal and infrasonic methods previously described are used here to analyse the kinematics of a PDC formed on 10 September 2010 by gravitational instability of the

277 remaining lava dome at SHV. The source of the PDC was on the
 278 western side of the headwall of the amphitheatre-shaped scar,
 279 formed by the partial dome collapse on 11 February 2010. PDCs
 280 are routinely detected by the thermal camera and are easily recog-
 281 nized in the imagery because of their higher temperature with
 282 respect to the background level (Fig. 9.3). The method of image
 283 decomposition is applied to track the propagation fronts of the
 284 PDC (Fig. 9.2), and to estimate displacement vectors in both the
 285 horizontal and vertical component. Once the image pixels are
 286 converted to metres, we may calculate the apparent movement of
 287 the PDC front, which in this case is 960 m in the horizontal direc-
 288 tion and 280 m in the vertical over 38 s (Fig. 9.4). Thus, we calcu-
 289 late the mean absolute apparent velocity of propagation as 26 m/s.
 290 Thermal image processing indicates a peak flow velocity of about
 291 65 m/s at the onset of the PDC (Fig. 9.5a). Over the following 15 s
 292 the PDC showed a rapid deceleration down to a constant value
 293 of about 20 m s^{-1} . During the successive 20 s, the PDC moved
 294 downhill at an almost constant velocity of around 20 m s^{-1}
 295 (Fig. 9.5a). The transition between the rapid deceleration and the
 296 constant velocity regimes is marked by a change of slope in the
 297 topography (Fig. 9.5d), and thus suggests a topographical control
 298 on the PDC dynamics.

299 These thermally derived PDC peak and mean velocities are con-
 300 sistent with previous estimates (Wadge *et al.* 1998; Calder *et al.*
 301 1999; Hooper & Mattioli 2001; Formenti *et al.* 2003; Ripepe
 302 *et al.* 2010).

303 Thermal images for the same PDC show a second moving front
 304 in the horizontal and vertical directions (frames 3–6 of Fig. 9.3). In
 305 particular, for the PDC in Figure 9.3, thermal images show at
 306 01:23:24 (frame 3) a NE-flowing high-temperature anomaly that
 307 is related to a second PDC following the main thermal front that
 308 occurred at 01:23:13. For this second PDC, the thermal camera
 309 detected displacement of 420 m in the horizontal and 100 m in
 310 the vertical directions, giving a total of approximately 432 m of
 311 displacement in 25 s (from 01:23:24 to 01:23:49) and an average
 312 velocity of around 17 m s^{-1} (Figs 9.4 & 9.5).

313
 314
 315



316
 317
 318
 319
 320
 321
 322
 323
 324
 325
 326
 327
 328
 329
 330
 331
 332
 333
 334
 335
 336
 337
 338
 339
Fig. 9.4. Temperature distribution along (a) the horizontal (H_d) and (b) the
 340 vertical (V_d) thermal image axes plotted as a function of time. This analysis
 341 allows tracking of the thermal fronts (black dots) along the vertical and the
 342 horizontal directions, and the calculation of their propagation velocities. White
 343 vertical lines with the associated numbering refer to the thermal snapshots
 344 shown in Figure 9.3.
 345

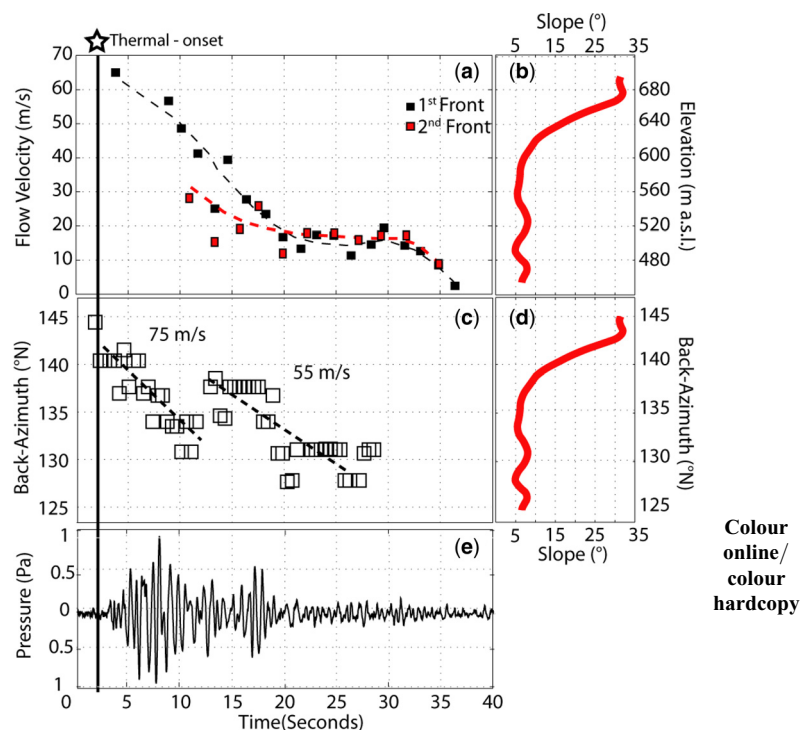


Fig. 9.5. (a) Thermal-derived velocity time-history of the two PDCs detected in
 the thermal images of Figure 9.3 are compared to (b) the infrasonic
 back-azimuth of (c) the associated infrasonic record. Thermal and acoustic
 analyses are both indicating a source that is moving from the dome to the NE
 with initial velocities of between 65 and 75 m s^{-1} . This velocity decreases after
 about 900 m (back-azimuth 131°N) from the dome down to approximately
 20 m s^{-1} , which coincides with (d & e) the slope changes in the topography and
 a stable infrasonic back-azimuth.

Infrasonic waves in the 0.7–3 Hz frequency range related to
 PDCs have been previously measured on Unzen and SHV volca-
 noes (Yamasato 1997; Oshima & Maekawa 2001; Ripepe *et al.*
 2010), and have been explained as being produced by the displace-
 ment of the atmosphere caused by the migration of the PDC front
 down the volcano's flank. The infrasound signal associated with
 the 10 September 2010 PDC event shows an emergent signal
 with peak amplitude of about 1 Pa at 5600 m from the source
 (Fig. 9.5c). Array processing shows coherent arrivals lasting for
 28 s (Fig. 9.5b), with a shift in the first event's back-azimuth
 from 142°N to 130°N occurring in 11.4 s, from 01:23:28 to
 01:23:39. At a slant distance of 5600 m, this back-azimuth shift
 towards the NE corresponds to a distance of 855 m, giving an
 apparent velocity of around 75 m s^{-1} . Considering a back-azimuth
 resolution of 0.9° that corresponds to 88 m at the dome, we can
 estimate an error in the velocity estimates of less than $\pm 8\%$.

Following this, the infrasonic back-azimuth jumps back to
 139°N and then shifts again toward the NE to 130°N in 10.4 s.
 This second shift in the back-azimuth indicates that a second
 PDC was generated that moved at an apparent velocity of about
 55 m s^{-1} . After that, the back-azimuth remains almost constant,
 ranging between 128°N and 134°N around an average direction
 of 131°N . This direction does not coincide with the dome but
 seems more associated with the change in the slope of the topogra-
 phical profile (Fig. 9.5d, e), suggesting that infrasound could be
 generated by the deceleration of the flow as it moved downhill.
 If we consider that the total shift of the infrasonic back-azimuth
 from 142°N to 128°N corresponds to a movement of 980 m over
 28 s, then this is consistent with a downhill propagation of the
 PDC at a mean velocity of approximately 35 m s^{-1} .

Infrasound and thermal image analysis are consistent with
 PDC dynamics characterized by two propagation fronts moving

346 toward the NE at a mean velocity ranging between 20 and
 347 35 m s^{-1} , and with a peak initial down-slope velocity of
 348 $55\text{--}75 \text{ m s}^{-1}$ (Fig. 9.5b, c).
 349

351 Thermal and acoustic observation of a Vulcanian 352 explosion

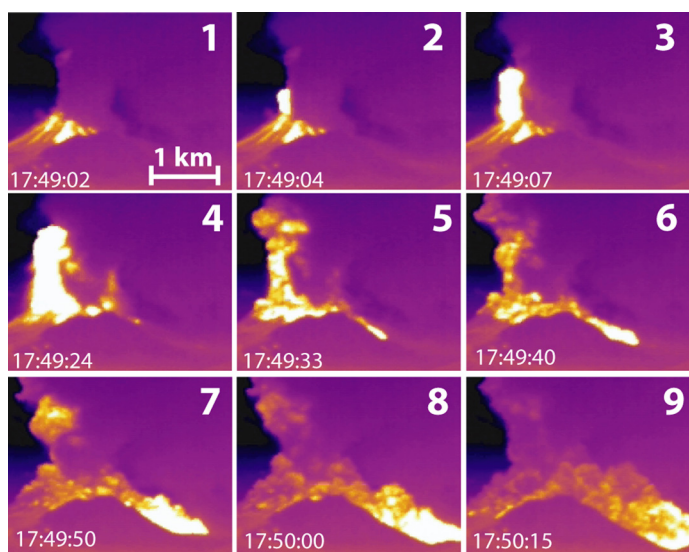
353
 354 Combined analysis of acoustic and thermal images can also
 355 provide valuable information on the dynamics of eruptive
 356 columns (Yokoo & Iguchi 2010; Delle Donne & Ripepe 2012).
 357 Both techniques can be used to constrain the eruptive onset,
 358 plume exit velocity and volumetric flux. Furthermore, the corre-
 359 lation of infrasound with thermal imagery can provide an impor-
 360 tant contribution to interpreting the associated seismic activity.
 361 Here we present the results of real-time processing of infrasound
 362 and thermal data associated with a Vulcanian explosion occurring
 363 at around 17:49 UTC on 5 February 2010 (Fig. 9.6). The seismic
 364 signal associated with this event lasted approximately 7 min,
 365 sending a tephra column to an elevation of 7.3 km above sea
 366 level (asl) into the atmosphere (Cole *et al.* 2014). Direct ob-
 367 servations showed extensive ballistic fragments showering the north-
 368 ern and western flanks of the volcano up to distances of around
 369 1 km. The vent area of the explosion was the western side of the
 370 lava-dome summit. The largest PDC associated with this explosion
 371 reached the sea (run-out of $>4 \text{ km}$) at Aymers Ghaut, and minor
 372 PDC activity (run-out of $<2 \text{ km}$) also occurred in several other
 373 valleys, including Tyre's Ghaut (Cole *et al.* 2014).
 374

375 Thermal image analysis

376
 377 The thermal camera imagery captured the main phases of the
 378 explosion dynamics (Fig. 9.6), with the initial injection of tephra
 379 into the atmosphere (frames 1–4) at 17:49:02, followed by
 380 plume collapse at 17:49:36 (frames 4–9). It is of note that
 381 within about 22 s of the onset (frame 4) the thermal camera
 382 shows a decrease in the integrated temperature in the FOV, indicat-
 383 ing that the tephra-column cooling related to a convective air
 384 entrainment mechanism and/or to an increase of cold ash in the
 385 atmosphere, which was preventing the detection of the volcanic
 386 activity at the dome.
 387

Q2

388 Explosive eruptions are generally described by two main gas
 389 dynamic phases. During the first phase, the volcanic plume is



390
 391
 392
 393
 394
 395
 396
 397
 398
 399
 400
 401
 402
 403
 404
 405
 406
 407
 408
 409
 410
 411
 412
 413
 414
Fig. 9.6. Thermal snapshots related to the Vulcanian eruption that occurred on 5 February 2010. The thermal gas-thrust phase is represented in the frames 1–4, after which the volcanic plume starts to collapse, generating large PDCs.

driven into the atmosphere by the gas thrust. Following this, the plume keeps rising at a relatively constant velocity by buoyancy, slowly expanding into the atmosphere while entraining air (Wilson 1980; Patrick 2007). The gas-thrust phase feeds hot tephra into the plume and is responsible for the increase in the temperature within the thermal camera FOV. The buoyancy phase is, however, associated with the reduction in the temperature in the FOV as no new volcanic material is ejected, but, rather, the plume rises at constant velocity by convective air entrainment with a consequent reduction of its internal temperature (Wilson 1980; Patrick 2007; Marchetti *et al.* 2009; Delle Donne & Ripepe 2012).

Q2

Thermal analysis provides the vertical rise velocity of the eruptive plume front, and the time-history of the plume-integrated temperature (Fig. 9.7e, f). This analysis shows that this Vulcanian

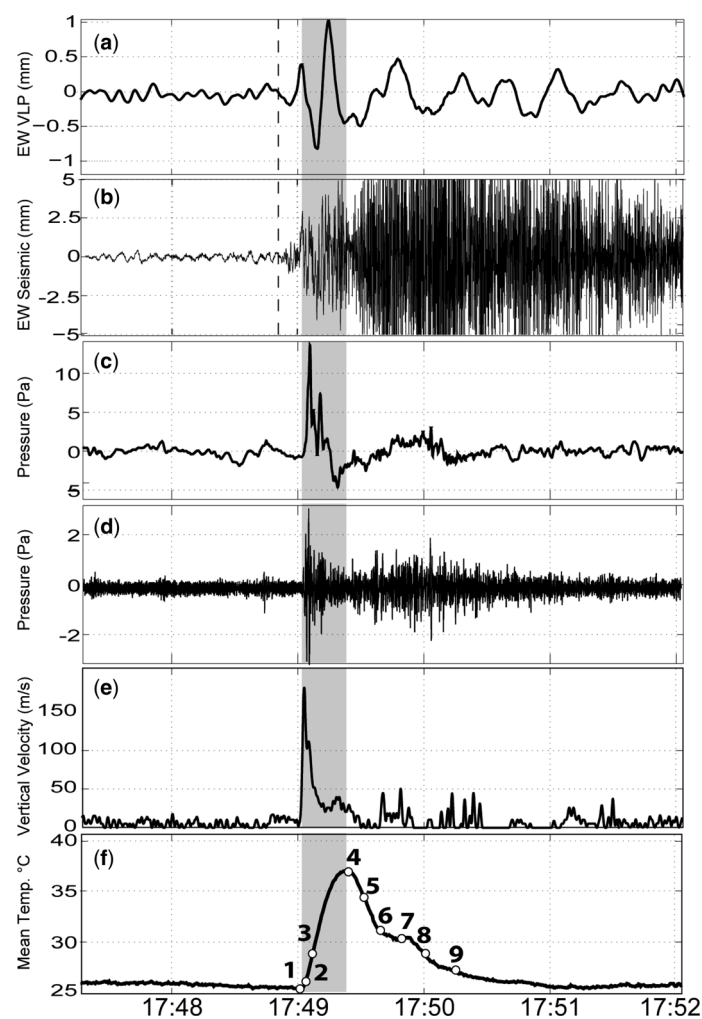


Fig. 9.7. Seismic-, acoustic- and thermal-derived signals associated with the 5 February 2010 Vulcanian eruption. (a) Seismic VLP ground displacement (using non-causal filter of Fig. 9.8) associated with the eruption onset. This signal is not evident but is still visible in the raw data (b), which have a strong high-frequency (1–20 Hz) amplitude component. Seismic onset is highlighted by the dashed black line and preceding the explosion (thermal and infrasound) onset of 13 s. Infrasound filtered between 0.2 and 20 Hz (d) indicate a high-frequency cigar-shape signal associated with PDC activity induced by the plume collapse that is correlated with the high-frequency seismic signal (b). Unfiltered infrasound (c) and thermal camera image processing (e, plume velocity; f, mean temperature) detected the eruption onset at 17:49:02, which was characterized by an exit velocity of 170 m s^{-1} (e) and a sharp positive compressive acoustic signal (c). Temperature (f) above the vent increased for approximately 13 s (point 4) in agreement with the duration of the seismic VLP (a), infrasonic broadband compression (c) and plume velocity (e). We suggest this is the duration of the eruptive gas-thrust phase (grey area) followed by the plume collapse and the generation of the PDCs.

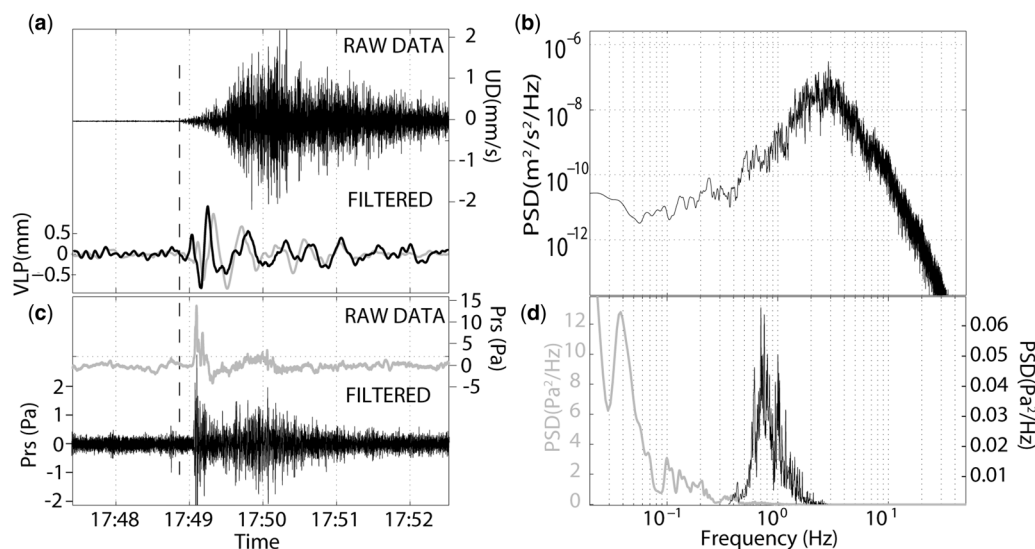


Fig. 9.8. (a) (top) Raw seismic ground velocity associated with the Vulcanian explosion of 5 February 2010 and recorded at MBGH shows (b) the main spectral energy in the 1–10 Hz frequency range peaked at 3 Hz. (a) (bottom) Seismic displacement, filtered using a causal (grey line) and non-causal (black line) filter between 0.03 and 0.1 Hz, contains a VLP event at 0.07 Hz, which has the maximum amplitude correlated with the eruption onset and the acoustic positive compressive signal (c) (top) with a frequency of 0.04 Hz (d, grey line). Infrasound filtered in the 0.2–20 Hz range (c, black line) shows a main frequency peak at 0.7 Hz (d, black line) consistent with the acoustic signal generated by PDCs, and coincident with the high-amplitude phase of the seismic ground velocity.

explosion is characterized by the ejection of gas and fragments into the atmosphere with initial velocities of about 170 m s^{-1} , which is followed by a sharp deceleration phase lasting approximately 13 s. The plume velocity becomes nearly constant at around 27 m s^{-1} , during which the gas thrust is still feeding the plume for about other 9 s, as also evidenced by the progressive increase of the integrated temperature (Fig. 9.7e, f, grey marked phase) for a total duration of 22 s. These plume velocities are fully consistent with previous estimates of $40\text{--}140 \text{ m s}^{-1}$ using image analysis of video camera records for several Vulcanian explosions occurring at SHV during the 1997 eruptive sequence (Druitt *et al.* 2002; Formenti *et al.* 2003).

At the end of the gas-thrust phase, the eruptive dynamics are marked by the collapse of the plume that generates impressive PDCs (frames 4–9 in Fig. 9.6), which reached the sea with a run-out of $>4 \text{ km}$. We interpret this collapse as being responsible for the decrease in the integrated temperature in the thermal trace (Fig. 9.7).

Infrasound and seismic records

This Vulcanian explosion was recorded both with the MVO broadband seismic network and with the infrasonic sensor at the MBFL station at the MVO (Fig. 9.8). The seismic signal shows a main duration of about 7 min (Fig. 9.8a), which includes both the pre-eruptive phase, the gas-thrust phase (i.e. injection of tephra into the atmosphere) and the plume collapse with the propagation of the PDCs.

There is no clear evidence of these different phases in the seismic waveform (Fig. 9.8a). The seismic signal was recorded at the St George's Hill station (MBGH), which is equipped with a broadband, three-component Guralp CGM-40 T seismometer ($T = 30 \text{ s}$). The signal shows an emergent onset reaching the maximum amplitude after approximately 60 s. Frequency content shows that the main spectral energy is confined in the 1–10 Hz frequency band (Fig. 9.8b). From the seismic ground velocity alone it is, thus, almost impossible to define when the explosion started and to distinguish between different phases of the eruptive dynamics (e.g. De Angelis *et al.* 2007).

The acoustic pressure can be explained as the rate of change of the volumetric outflow (Lighthill 1978). When a volumetric source

is expanding, it will produce an equivalent displacement of the overlying atmosphere, and initiate an acoustic wave. An acoustic pressure pulse can be caused by magma accelerating and pushing atmosphere aside at the vent. The duration of an acoustic signal may be indicative of the duration of the gas-thrust phase during the explosive process.

Infrasound recorded 5600 m from the dome clearly marks the explosion onset as a sharp positive pressure peak of 14 Pa, that would give approximately 0.8 bar of excess pressure if reduced to 1 m from the vent (Fig. 9.8c). The acoustic signal therefore allows us to mark the exact time at which the volcanic plume interacts with the atmosphere. Considering a sound speed of 340 m s^{-1} , we adjust the 17:49:19 arrival time at the MVO by 16.47 s, which sets the origin time at 17:49:02. This is consistent with the timing of the thermal image record (Fig. 9.7d, f) used to define the explosion onset.

Dynamics of the eruptive plume

In order to compare the seismic and infrasonic data we adjusted the arrival time of the seismic signal by the distance between the station MBGH and the SHV dome (3880 m). Considering a mean seismic velocity of 2500 m s^{-1} (Luckett *et al.* 2007), this distance converts to a propagation time of 1.55 s. The emergent onset of the seismic ground velocity, once converted for the propagation time, starts at 17:48:49, which is approximately 13 s before the acoustic onset (dashed line Fig. 9.8a–c) and indicates a pre-eruptive dynamics that may be related to the pressurization of the conduit before the explosion onset (Green & Neuberg 2005).

Seismic and infrasonic data have been filtered in order to emphasize different components of the eruptive process (Fig. 9.7a, b). The seismic signal converted in displacement and filtered (two poles, zero-phase, non-causal filter) in the 0.03–0.1 Hz frequency range shows a very long period (VLP) component with a frequency of 0.07 Hz. The origin time of this VLP seismic signal (dashed line in Figs 9.7a, b & 9.8a–c) coincides with the onset of the seismic unfiltered ground velocity (Fig. 9.8a, top). This approximately 13 s time delay is reduced to about 10 s when a causal filter is applied (e.g. Patrick *et al.* 2011) to the seismic displacement (grey line in Fig. 9.8a). However, we prefer to use a non-causal filter because it preserves the phase relationship

484 between the original and filtered seismic signals, as shown in
 485 Figure 9.7 a, b. The correlation between the VLP signal and the
 486 eruptive process is more evident when we compare the VLP
 487 signal with the infrasound (Fig. 9.7d).

488 Infrasound is characterized by a low-frequency spectral peak
 489 (Fig. 9.8d) at 0.04 Hz (25 s), and it clearly corresponds to the
 490 explosion onset with a sharp positive pressure peak lasting
 491 around 13 s. This compressive phase is followed by a longer nega-
 492 tive coda lasting 29 s.

493 The maximum amplitude of the VLP seismic displacement
 494 (independent of the filter used) coincides (grey marked area in
 495 Fig. 9.7) with the positive infrasonic peak, indicating that the
 496 VLP seismic signal originated during the initial gas-thrust phase
 497 of the explosion. The analysis of the thermal images reveals that
 498 the duration of the seismic and infrasonic signals coincides with
 499 the duration of the temperature increase (Fig. 9.7f) and with the
 500 plume velocity decrease from 170 m s^{-1} to a more constant
 501 plume flow of about 27 m s^{-1} . This time corresponds to frame 4
 502 in the thermal sequence of Figure 9.7, and marks the beginning
 503 of the column collapse and the onset of the PDCs. Thermal and
 504 acoustic data thus suggest that the VLP signal could be generated
 505 by a co-eruptive source represented by the downwards force of the
 506 explosion (Kanamori *et al.* 1984).

507 Seismic and acoustic signature of PDCs

508 PDCs at SHV are generally characterized by infrasound in the
 509 frequency range of between 0.4 and 2 Hz (Ripepe *et al.* 2010).
 510 We have filtered the infrasound above 0.2 Hz to highlight the
 511 contribution of the PDC (Fig. 9.7d). However, the explosive
 512 dynamics also radiate in this frequency band. The filtered
 513 signal shows a sharp infrasonic onset and a pressure peak of
 514 approximately 2.5 Pa. This initial signal dies out at the end of
 515 the gas-thrust phase but only after the peak of the thermal
 516 anomaly (Fig. 9.7f, grey marked area). After that, the infrasound
 517 decreases to a minimum amplitude (Fig. 9.7d), which is fol-
 518 lowed by a second phase of emergent and gradual amplitude
 519 increase up to 1 Pa. This second phase represents the infrasound
 520 generated by the PDCs, and coincides with the duration and
 521 shape of the seismic signal (Fig. 9.7a). This similarity indicates
 522 that the seismic signal is dominated by a frequency band above
 523 1 Hz related to PDC activity more than by the explosive process.
 524 Moreover, the duration of the high-frequency seismic signal of
 525 approximately 7 min coincides to the duration of the infrasound
 526 above 1 Hz.

527 This PDC moving westwards was also detected by thermal
 528 camera (Fig. 9.6, frames 6–9), and the propagation vector of the
 529 PDC front was calculated by using the previously described
 530 thermal image decomposition method (Fig. 9.9a). Front velocities
 531 range between 15 and 65 m s^{-1} (Fig. 9.9b), and show a deceleration
 532 from 40 to 15 m s^{-1} during approximately the first 15 s followed
 533 by a marked acceleration up to 65 m s^{-1} in the following
 534 12 s (Fig. 9.9b). We suggest that this velocity profile reflects two
 535 separate PDC events. We propose that an initial small PDC, possi-
 536 bly associated with a minor gravitational collapse of the lava
 537 dome, occurred during the initial part of the explosion, and was
 538 followed about 15 s later by a larger and more energetic PDC gener-
 539 ated by the collapse of the tephra column.

540 Summary and conclusions

541 Extrusion of andesite lava at SHV is associated with violent Vul-
 542 canian explosions that transport large quantities of tephra to
 543 heights of tens of kilometres into the atmosphere. The collapse
 544 of tephra columns during explosions and the instability of lava
 545 domes are the cause of PDC activity. We have shown how a
 546 thermal camera and an infrasonic array provide valuable

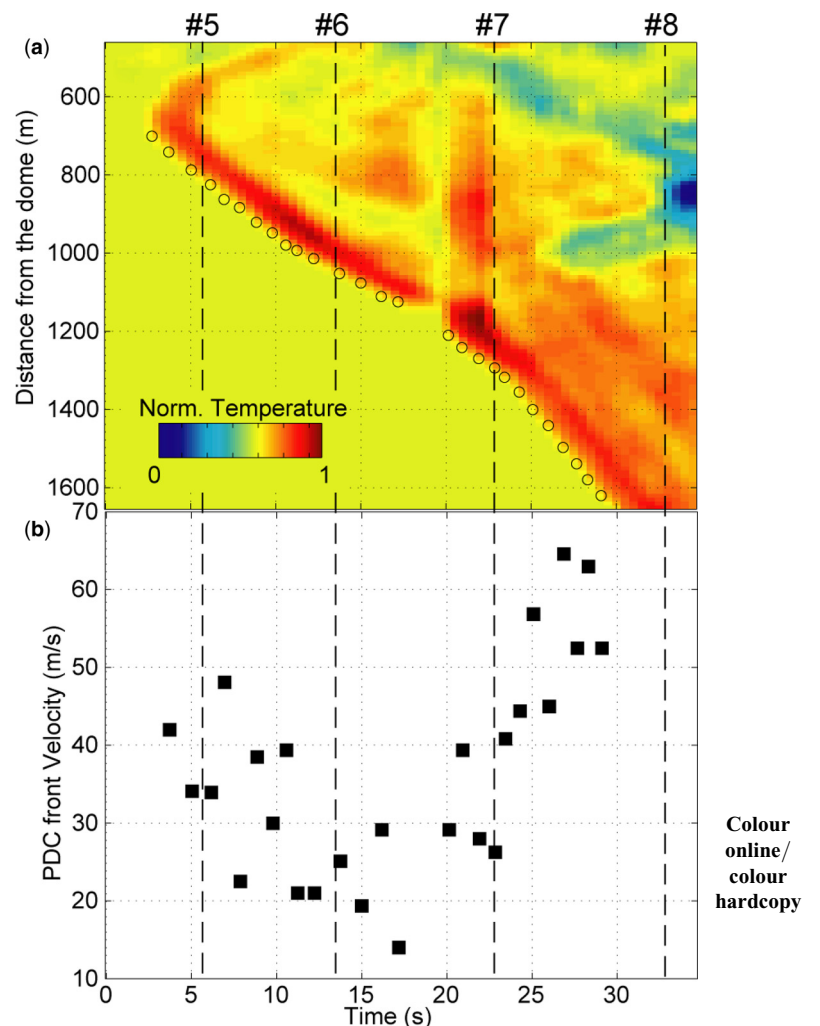


Fig. 9.9. (a) Normalized temperature distribution and (b) velocity profile associated with the PDC front produced by 5 February 2010 Vulcanian explosion. Vertical dashed lines and associated numbering are relative to the frames of the thermal images of Figure 9.6. PDC travels westwards with an initial velocity of 40 m s^{-1} , decelerating to 15 m s^{-1} during approximately the first 15 s, and then accelerating up to 65 m s^{-1} in the following 12 s. We interpret this as the evidence of two different PDCs generated by the initial small-dome collapse produced by the explosive dynamics, followed by a larger PDC associated with the ash-plume collapse.

information that can track and quantify both phenomena. These techniques improve the ability of the MVO to detect and to monitor these phenomena in real time providing the foundation for a reliable risk assessment.

Thermal and infrasonic monitoring techniques allow detection of PDCs, and real-time tracking of their propagation vectors both in terms of flow direction and downhill velocity. In particular, we found that the velocity of the PDCs determined from both thermal and infrasonic data processing show comparable values, with an initial peak velocity of the order of approximately 55 – 75 to 20 m s^{-1} within about the first 17 s. Thermal camera 2D images were back-projected onto a DEM, allowing location of the thermal anomaly onto 3D topography. From a monitoring point of view, this improves the ability to visualize the flow run-out in real time, even in poor visibility or at night. However, no infrasound is detected for back-azimuths of less than 127°N . The velocity of the PDC front derived by thermal images indicates that this infrasonic back-azimuth coincides with a constant PDC velocity at approximately 20 m s^{-1} (Fig. 9.5). Although our DEM refers to 2008 topography, in which the depression of the 2010 collapse scar is not represented, the 3D thermal images

(Fig. 9.3) suggest that the 127°N infrasonic back-azimuth and the deceleration of the PDC front could coincide with a slope change in the topography (Fig. 9.5c). Infrasonic associated with the PDC seems to be produced by the rapid changes of the PDC front velocity induced by topography.

Infrasonic data and thermal camera imagery allow the identification of the onset of Vulcanian explosions and provides constraints on the different phases of the explosive dynamics. This information is more difficult to extract from seismic signals alone, and thus thermal images and infrasonic can help in the interpretation of explosion dynamics. In the case of the 5 February 2010 explosion, thermal camera imagery reveals a temperature increase above the dome lasting for 22 s, which coincides with the onset and the duration of the positive compressive infrasonic signal in the low-frequency band <1 Hz. Furthermore, thermal decomposition of the camera imagery shows a rapid deceleration of the plume velocity from the initial approximately 170 m s⁻¹ to a more constant ascent rate of around 27 m s⁻¹.

We attribute this initial eruptive phase as being dominated by the gas-thrust feeding tephra into the atmosphere with a velocity, $U(t)$, which gives an average volumetric discharge rate, $\Phi(t) = \pi R^2 U(t)$, ranging between 3.3×10^4 and 9.2×10^5 m³ s⁻¹, assuming a vent radius, R , of between 15 and 25 m based on the dimensions of spines extruded from the dome (Watts *et al.* 2002). To estimate the mass flux we need to know density of the plume. This parameter can be achieved by fall-out distribution and tephra dispersal analysis. Estimations of plume density in Vulcanian explosions with comparable magnitude are given by Ripepe & Harris (2008) and by Pistolesi *et al.* (2011) for the 5 April 2003 and 15 March 2007 Stromboli explosions, respectively. For these explosions, authors estimate a plume density of 6.7 and 13.5 kg m⁻³, respectively. Using these plume-density values, the mass fluxes of the 5 February 2010 explosion at SHV would be between 0.2×10^6 and 13.3×10^6 kg s⁻¹. Accordingly, the total discharged plume volume of $0.8 \times 10^6 - 20.2 \times 10^6$ m³ is estimated by integrating the volume flux on the 22 s-long gas-thrust phase, that would give a total discharged mass of $5.4 \times 10^6 - 272 \times 10^6$ kg. This is in agreement with previous estimates using different methods from other Vulcanian eruptions at SHV (Druitt *et al.* 2002; Formenti *et al.* 2003; Komorowski *et al.* 2010; Cole *et al.* 2014).

The seismic signal associated with the gas-thrust phase becomes evident only when filtered below 0.1 Hz in the 0.03–0.1 frequency band. This VLP seismic signal with a frequency of 0.04 Hz seems to be a typical feature of large Vulcanian explosions at SHV, at least in the 2008–2010 period (Cole *et al.* 2013), but not previously reported. Nevertheless, ultra-low-period (ULP > 100 s) seismic signals have been recorded by broadband seismometers at SHV (Green & Neuberg 2005) and explained as being related to the pressurization of the upper conduit, presumably by a trapped gas phase.

The fragmentation of overpressurized magmatic foam allows rapid expansion of the magma in the conduit driving material out the vent and into the atmosphere. The ground will react to a change in the upwards momentum induced by the mass discharge with a downwards-orientated counter force (Kanamori *et al.* 1984), which is probably the source of the VLP seismic signal. The correlation with the plume velocity derived by thermal image analysis (Fig. 9.7a, e) seems to support this interpretation.

When eruptive dynamics are no longer able to sustain the column, ejection velocity drops down to 10 m s⁻¹ (Fig. 9.7e) and the plume collapses generating PDCs (Fig. 9.6, frames 4–10). Infrasonic above 0.2 Hz reveals a high-frequency emergent signal at 0.7 Hz reaching maximum pressure amplitude approximately 60 s after the eruption onset (Fig. 9.7d). The seismic signal mimics the infrasonic waveform, suggesting that the PDC source is strongly coupled with both the atmosphere and the ground. This indicates that the seismic signal above 1 Hz is not related to the explosive dynamics but is rather caused by the

PDC activity. Therefore, the amplitude and duration of the seismic signal (>1 Hz) is not related to the energy and the duration of the explosive process, but, rather, they are related to the amplitude and duration of PDCs that were generated during the plume collapse.

We thank C. 'Pyiko' Williams, N. Fournier and A. Finizola for invaluable support in the field and the scientific discussions on thermal images and acoustic waves. The manuscript has been improved by the critical comments of M. Patrick and J. Johnson.

References

- BOOKSTEIN, F. L. 1989. Principal warps: thin-plate splines and the decomposition of deformations. *IEEE Transactions on Pattern Analysis and Machine Intelligence*, **11**, 567–585.
- CALDER, E. S., COLE, P. D. *ET AL.* 1999. Mobility of Pyroclastic Flows and Surges at the Soufrière Hills Volcano, Montserrat. *Geophysical Research Letters*, **26**, 537–540 <http://dx.doi.org/10.1029/1999GL900051>
- CALDER, E. S., LUCKETT, R., SPARKS, R. S. J. & VOIGHT, B. 2002. Mechanisms of lava dome instability and generation of rock-falls and pyroclastic flows at Soufrière Hills Volcano, Montserrat. *In: DRUITT, T. H. & KOKELAAR, B. P. (eds) The Eruption of Soufrière Hills Volcano, Montserrat, from 1995 to 1999*. Geological Society, London, Memoirs, **21**, 173–190.
- CANSI, Y. 1995. An automatic seismic event processing for detection and location; the P.M.C.C. method. *Geophysical Research Letters*, **22**, 1021–1024.
- CARN, S. A., WATTS, R. B., THOMPSON, G. & NORTON, G. E. 2004. Anatomy of a Lava Dome Collapse: the 20 March 2000 Event at Soufrière Hills Volcano, Montserrat. *Journal of Volcanology and Geothermal Research*, **131**, 241–264, [http://dx.doi.org/10.1016/S0377-0273\(03\)00364-0](http://dx.doi.org/10.1016/S0377-0273(03)00364-0)
- COLE, P. D., CALDER, E. S. *ET AL.* 2002. Deposits from dome-collapse and fountain-collapse pyroclastic flows at Soufrière Hills Volcano, Montserrat. *In: DRUITT, T. H. & KOKELAAR, B. P. (eds) The Eruption of Soufrière Hills Volcano, Montserrat, from 1995 to 1999*. Geological Society London, Memoirs, **21**, 231–262.
- COLE, P. D., SMITH, P. J., STINTON, A. J., ODBERT, H. M., BERNSTEIN, M. L., KOMOROWSKI, J. C. & STEWART, R. 2014. Vulcanian explosions at Soufrière Hills Volcano, Montserrat between 2008 and 2010. *In: WADGE, G., ROBERTSON, R. E. A. & VOIGHT, B. (eds) The Eruption of Soufrière Hills Volcano, Montserrat from 2000 to 2010*. Geological Society, London, Memoirs, **39**, 93–109, <http://dx.doi.org/10.1144/M39.5>
- DE ANGELIS, S., BASS, V., HARDS, V. & RYAN, G. 2007. Seismic characterization of pyroclastic flow activity at Soufrière Hills Volcano, Montserrat, 8 January 2007. *Natural Hazards Earth Systems Science*, **7**, 467–472.
- DELLE DONNE, D. & RIPEPE, M. 2012. High-frame rate thermal imagery of Strombolian explosions: implications for explosive and infrasonic source dynamics. *Journal of Geophysical Research*, **117**, B09206, <http://dx.doi.org/10.1029/2011JB008987>
- DRUITT, T., YOUNG, S. *ET AL.* 2002. Episodes of cyclic Vulcanian explosive activity with fountain collapse at Soufrière Hills Volcano, Montserrat. *In: DRUITT, T. & KOKELAAR, B. (eds) The Eruption of Soufrière Hills Volcano, Montserrat, from 1995 to 1999*. Geological Society, London, Memoirs, **21**, 281–306.
- FORMENTI, Y., DRUITT, T. H. & KELFOUN, K. 2003. Characterisation of the 1997 Vulcanian explosions of Soufrière Hills Volcano, Montserrat, by video analysis. *Bulletin of Volcanology*, **65**, 587–605, <http://dx.doi.org/10.1007/s00445-003-0288-8>
- GARCÉS, M. A., IGUCHI, M., ISHIHARA, K., MORRISSEY, M., SUDO, Y. & TSUTSUI, T. 1999. Infrasonic precursors to a Vulcanian eruption at Sakurajima Volcano, Japan. *Geophysical Research Letters*, **26**, 2537–2540.
- GARCÉS, M. A., McNUTT, S. R., HANSEN, R. A. & EICHELBERGER, J. C. 2000. Application of wave-theoretical seismoacoustic models to the interpretation of explosion and eruption tremor signals radiated by

- 622 Pavlov Volcano, Alaska. *Journal of Geophysical Research*, **105**,
623 3039–3058.
- 624 GREEN, D. N. & NEUBERG, J. 2005. Seismic and infrasonic signals associ-
625 ated with an unusual collapse event at the Soufrière Hills volcano,
626 Montserrat. *Geophysical Research Letters*, **32**, L07308, <http://dx.doi.org/10.1029/2004GL022265>
- 627 HOOPER, D. M. & MATTIOLI, G. S. 2001. Kinematic modeling of
628 pyroclastic flows produced by gravitational Dome Collapse at Sou-
629 frière Hills Volcano, Montserrat. *Natural Hazards*, **23**, 65–86.
- 630 JOLLY, A. D., THOMPSON, G. & NORTON, G. E. 2002. Locating pyro-
631 clastic flows on Soufrière Hills Volcano, Montserrat, West Indies,
632 using amplitude signals from high dynamic range instru-
633 ments. *Journal of Volcanology and Geothermal Research*, **118**,
634 299–317.
- 635 JOHNSON, J. B. 2007. On the relation between infrasound, seismicity, and
636 small pyroclastic explosions at Karymsky Volcano. *Journal of*
637 *Geophysical Research*, **112**, B08203, [http://dx.doi.org/10.1029/](http://dx.doi.org/10.1029/2006JB004654)
638 [2006JB004654](http://dx.doi.org/10.1029/2006JB004654)
- 639 JOHNSON, J. B. & RIPEPE, M. 2011. Volcano Infrasound: a review. *Journal*
640 *of Volcanology and Geothermal Research*, **206**, 61–69, <http://dx.doi.org/10.1016/j.jvolgeores.2011.06.006>
- 641 KANAMORI, H., GIVEN, J. W. & LAY, T. 1984. Analysis of seismic body
642 waves excited by the Mount St. Helens eruption of May 18, 1980.
643 *Journal of Geophysical Research*, **89**, 1856–1866.
- 644 KOMOROWSKI, J. C., LEGENDRE, Y. ET AL. 2010. Insights into processes
645 and deposits of hazardous vulcanian explosions at Soufrière Hills
646 Volcano during 2008 and 2009 (Montserrat, West Indies). *Geophys-
647 ical Research Letters*, **37**, L00E19, [http://dx.doi.org/10.1029/](http://dx.doi.org/10.1029/2010GL042558)
648 [2010GL042558](http://dx.doi.org/10.1029/2010GL042558)
- 649 LIGHTHILL, M. J. 1978. *Waves in Fluids*. Cambridge University Press,
650 New York.
- 651 LUCKETT, R., BAPTIE, B. & OTTEMOLLER, L. 2007. Seismic monitoring at
652 Soufrière Hills Volcano, Montserrat. *Seismological Research Letters*,
653 **78**, 192–200, <http://dx.doi.org/10.1785/gssrl.78.2.192>
- 654 MARCHETTI, E., RIPEPE, M., HARRIS, A. J. L. & DELLE DONNE, D. 2009.
655 Tracing the differences between Vulcanian and Strombolian
656 explosions using infrasonic and thermal radiation energy. *Earth Pla-
657 netary Science Letters*, **279**, 273–281, [http://dx.doi.org/10.1016/](http://dx.doi.org/10.1016/j.epsl.2009.01.004)
658 [j.epsl.2009.01.004](http://dx.doi.org/10.1016/j.epsl.2009.01.004)
- 659 NIKOLKINA, I., ZAHIBO, N., TALIPOVA, T. & PELINOVSKY, E. 2011. Pyro-
660 clastic flow from Soufrière Hills Volcano, Montserrat: Solid Block
661 Model. *International Journal of Geosciences*, **2**, 326–335.
- 662 OSHIMA, H. & MAEKAWA, T. 2001. Excitation process of infrasonic waves
663 associated with Merapi-type pyroclastic flow as revealed by a new
664 recording system. *Geophysical Research Letters*, **28**, 1099–1102.
- 665 PATRICK, M. R. 2007. Dynamics of Strombolian ash plumes from
666 thermal video: motion, morphology, and air entrainment. *Journal of*
667 *Geophysical Research*, **112**, B06202, [http://dx.doi.org/10.1029/](http://dx.doi.org/10.1029/2006JB004387)
668 [2006JB004387](http://dx.doi.org/10.1029/2006JB004387)
- 669 PATRICK, M. R., WILSON, D., FEE, D., ORR, T. & SWANSON, D. 2011.
670 Shallow degassing events as a trigger for very-long-period seismicity
671 at Kīlauea Volcano, Hawai'i. *Bulletin of Volcanology*, **73**,
672 1179–1186, <http://dx.doi.org/10.1007/s00445-011-0475-y>
- 673 PISTOLESI, M., DELLE DONNE, D., PIOLI, L., ROSI, M. & RIPEPE, M. 2011.
674 The 15 March 2007 explosive crisis at Stromboli Volcano, Italy:
675 assessing physical parameters through a multidisciplinary approach.
676 *Journal of Geophysical Research*, **116**, B12206, [http://dx.doi.org/](http://dx.doi.org/10.1029/2011JB008527)
677 [10.1029/2011JB008527](http://dx.doi.org/10.1029/2011JB008527)
- 678 RIPEPE, M. & HARRIS, A. J. L. 2008. Dynamics of the 5 April 2003 explo-
679 sive paroxysm observed at Stromboli by a near-vent thermal, seismic
680 and infrasonic array. *Geophysical Research Letters*, **35**, L07306,
681 <http://dx.doi.org/10.1029/2007GL032533>
- 682 RIPEPE, M., MARCHETTI, E. & ULIVIERI, G. 2007. Infrasonic monitoring
683 at Stromboli volcano during the 2003 effusive eruption: insights on
684 the explosive and degassing process of an open conduit system.
685 *Journal of Geophysical Research*, **112**, B09207, [http://dx.doi.org/](http://dx.doi.org/10.1029/2006JB004613)
686 [10.1029/2006JB004613](http://dx.doi.org/10.1029/2006JB004613)
- 687 RIPEPE, M., DE ANGELIS, S. ET AL. 2009. Tracking Pyroclastic Flows
688 at Soufrière Hills Volcano. *Eos, Transactions of the American*
689 *Geophysical Union*, **90**, 229–230, [http://dx.doi.org/10.1029/](http://dx.doi.org/10.1029/2009EO270001)
690 [2009EO270001](http://dx.doi.org/10.1029/2009EO270001)
- 691 RIPEPE, M., DE ANGELIS, S., LACANNA, G. & VOIGHT, B. 2010. Obser-
692 vation of infrasonic and gravity waves at Soufrière Hills Volcano,
693 Montserrat. *Geophysical Research Letters*, **37**, L00E14, [http://dx.doi.org/10.1029/](http://dx.doi.org/10.1029/2010GL042557)
694 [2010GL042557](http://dx.doi.org/10.1029/2010GL042557)
- 695 SPARKS, R. S. J. & YOUNG, S. R. 2002. The eruption of Soufrière Hills
696 Volcano, Montserrat (1995–1999): overview of scientific results.
697 In: DRUITT, T. H. & KOKELAAR, B. P. (eds) *The Eruption of Soufrière*
698 *Hills Volcano, Montserrat, from 1995 to 1999*. Geological Society
699 London, Memoirs, **21**, 45–69.
- 700 ULIVIERI, G., MARCHETTI, E., RIPEPE, M., CHIAMBRETTI, I., DE ROSA, G.
701 & SEGOR, V. 2011. Monitoring snow avalanches in Northwestern
702 Italian Alps using an infrasound array. *Cold Regions Science and*
703 *Technology*, **69**, 177–183.
- 704 VERGNOLLE, S. & CAPLAN-AUERBACH, J. 2006. Basaltic thermals and
705 subplinian plumes: constraints from acoustic measurements at
706 Shishaldin volcano, Alaska. *Bulletin of Volcanology*, **68**, 611–630.
- 707 WADGE, G., JACKSON, P., BOWER, S. M., WOODS, W. & CALDER, E. 1998.
708 Computer simulations of pyroclastic flows from dome collapse.
709 *Geophysical Research Letters*, **25**, 3677–3680.
- 710 WATTS, R. B., HERD, R. A., SPARKS, R. S. J. & YOUNG, S. R. 2002.
711 Growth patterns and emplacement of the andesite lava dome at
712 Soufrière Hills Volcano, Montserrat. In: DRUITT, T. H. & KOKELAAR,
713 B. P. (eds) *The Eruption of Soufrière Hills Volcano, Montserrat,*
714 *from 1995 to 1999*. Geological Society London, Memoirs, **21**,
715 115–152.
- 716 WILSON, L. 1980. Relationships between pressure, volatile content and
717 ejecta velocity in three types of volcanic explosion. *Journal of Volca-
718 nology and Geothermal Research*, **8**, 297–313.
- 719 YAMASATO, H. 1997. Quantitative analysis of pyroclastic flows using infra-
720 sonic and seismic data at Unzen volcano, Japan. *Journal of Physics of*
721 *the Earth*, **45**, 397–416.
- 722 YOKOO, A. & IGUCHI, M. 2010. Using infrasound waves from eruption
723 video to explain ground deformation preceding the eruption of Suwa-
724 nosejima volcano, Japan. *Journal of Volcanology and Geothermal*
725 *Research*, **196**, 287–294.
- 726 YOUNG, S. R., SPARKS, R. S. J., ASPINALL, W. P., LYNCH, L. L., MILLER, A.
727 D., ROBERTSON, R. E. A. & SHEPHERD, J. B. 1998. Overview of the
728 eruption of Soufrière Hills volcano, Montserrat, July 18 1995 to
729 December 1997. *Geophysical Research Letters*, **25**, 3389–3392.